

Article

Flash-Boiling Spray Dynamics: Ethanol and Gasoline Compared through X-ray and Schlieren Diagnostics

Weidi Huang and Hongliang Luo *

College of Power and Energy Engineering, Harbin Engineering University, Harbin 150001, China

* Correspondence: luohl@hrbeu.edu.cn

Received: 22 March 2025; Revised: 2 April 2025; Accepted: 7 April 2025; Published: 9 April 2025

Abstract: Flash-boiling sprays in gasoline direct injection (GDI) engines play a pivotal role in achieving efficient fuel-air mixing, yet their dynamics under superheated conditions remain poorly understood, particularly for multi-component fuels. This study bridges this gap by employing advanced X-ray phase-contrast imaging (XPCI) and schlieren techniques to investigate ethanol and gasoline sprays, offering unprecedented insights into near-nozzle and downstream behaviors. The work reveals that ethanol's distinct single-component properties trigger unambiguous flash-boiling phenomena (e. g., plume merging, upward curling), while gasoline's complex composition suppresses homogeneous phase change, challenging conventional flash-boiling frameworks. XPCI captures persistent liquid cores near the nozzle exit under superheating—a critical yet overlooked feature—highlighting the interplay between inertial forces and vaporization kinetics. The study further demonstrates how flash boiling redistributes spray momentum, enhancing radial dispersion while reducing axial penetration, with implications for mitigating tip wetting and wall impingement. By correlating droplet size, velocity profiles, and phase-change dynamics, this research not only advances and refines the fundamental understanding of flash-boiling atomization but also provides actionable insights for optimizing combustion efficiency and reducing emissions in next-generation GDI engines.

Keywords: flash boiling spray; XPCI; schlieren imaging; ethanol; gasoline; primary breakup

1. Introduction

Flash-boiling sprays are critical to advancing gasoline direct injection (GDI) engine performance, as they enable superior fuel-air mixing and cleaner combustion by leveraging rapid vaporization under superheated conditions [1,2]. This phenomenon occurs when the in-cylinder ambient pressure drops below the fuel's saturation pressure, a scenario commonly encountered during hot part-load operation or advanced intake-valve-closing strategies. These conditions create a partial vacuum during injection, promoting spontaneous phase change and enhancing spray atomization [3].

While prior studies by Zeng et al. [4,5] and Wu et al. [6,7] have systematically characterized macroscopic spray behaviors—such as expanded cone angles, plume merging, and intensified droplet interactions—persistent challenges like nozzle tip wetting and piston impingement [8,9], highlighting unresolved complexities in balancing atomization efficiency and operational reliability.

Despite progress, fundamental gaps remain in understanding the primary breakup mechanisms governing flash-boiling sprays. Conventional models predominantly assume that bubble nucleation and growth within droplets drive fragmentation [10,11]. However, empirical validation of these assumptions is limited, particularly for high-speed sprays with ultrafine droplets (e. g., <100 μm), where thermal and dynamic non-equilibrium conditions dominate. Scaled-up experimental setups, often used to simplify observation, struggle to replicate the extreme pressure gradients and microscale interactions inherent to real-world sprays. Recent cryogenic flash-boiling studies by Loureiro et al. [12,13] further highlight these limitations, emphasizing discrepancies between idealized models and actual spray behavior.



Compounding this uncertainty, studies using transparent nozzles propose diverse atomization pathways. For instance, Oza [14] postulated a two-phase flow of vapor and droplets at the injector exit under specific pressures, while Bar-Kohany et al. [15] classified sprays into non-shattering, partial-shattering, and full-shattering regimes. The latter regime, characterized by negligible breakup lengths, directly contradicts traditional theories that attribute atomization to liquid-core instabilities.

Resolving these debates necessitates direct observation of near-nozzle dynamics in superheated sprays. To address this, we employ X-ray phase-contrast imaging (XPCI), a technique pioneered for fuel spray analysis in the early 2000s [16–18]. XPCI excels in resolving liquid-core structures due to its ultra-high energy and short wavelength, though it does not interact with the spray's gas phase. Leveraging this capability, this study investigates the behavior of droplets and liquid cores at the nozzle exit under flash-boiling conditions. By capturing high-fidelity, time-resolved images of the near-field spray region, we aim to elucidate the spray dynamics driving primary breakup and atomization. These insights will advance predictive models and inform strategies to mitigate adverse effects (e.g., tip wetting) while harnessing flash-boiling benefits for enhanced combustion efficiency in GDI engines.

2. Description of Experiments

2.1. Tested Fuels

This study used ethanol and gasoline for a comparing study. Figure 1 illustrates the distillation curves of both fuels at 1.0 bar, measured using an Automated Distillation Tester (Tanaka Scientific Limited AD-6 Type, Tokyo, Japan). Ethanol exhibits a single-stage distillation profile with a saturated temperature of 78 °C, while gasoline demonstrates a multi-stage distillation process, reaching full vaporization near 200 °C.

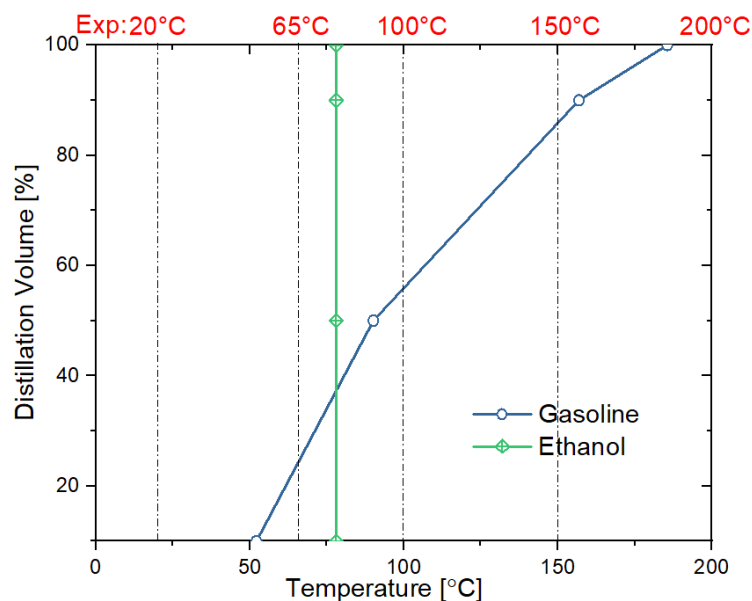


Figure 1. Distillation degree of testing fuels at 1.0 bar.

The key physical properties of ethanol and gasoline at room temperature (25 °C) and ambient pressure (1.0 bar) are summarized in Table 1. Fuel density and viscosity were measured using an Anton Paar DMA 4100M densimeter and a Yoshida-Kagaku VB-X6 (Kikai Co., Tokyo, Japan) viscometer, respectively. Surface tension values were obtained from literature [19], and latent heat of vaporization data were sourced from references [20,21].

Table 1. Fuel properties testing fuels (at 25 °C and ambient pressure).

Fuel Properties	Gasoline	Ethanol
Density [kg/m ³]	732.3	794.5
Viscosity [mPa·s]	0.411	1.244
Surface tension [mN/m]	22.3	22.9
Latent heat of vaporization [kJ/kg]	305	840

2.2. Testing Nozzle

For the investigation, a commercial Gasoline Direct Injection (GDI) injector was employed. This injector model features six holes, designed in a hole-and-counterbore configuration. Such a configuration is commonly utilized in GDI engines to facilitate enhanced spray breakup [22–24]. A schematic depiction of the internal structure of the test nozzle is presented in Figure 2, accompanied by a summary of its geometric parameters in Table 2. The red lines represent the projected axial positions of all nozzle holes on the cross-sectional plane. Notably, all holes within the injector possess identical diameters for both the hole and counterbore. However, the length of each hole varies depending on its inclining angle.

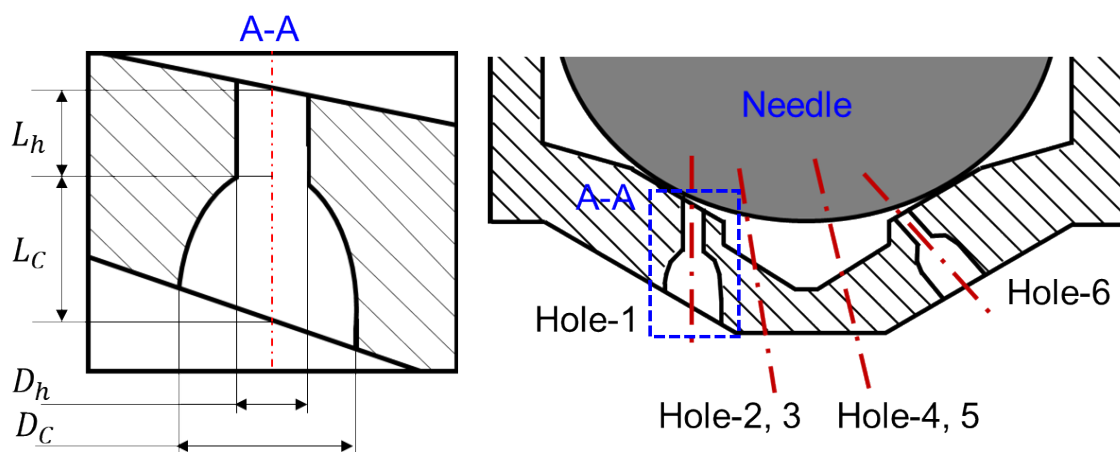


Figure 2. Nozzle internal structure and geometric parameters.

Table 2. Geometric parameters of the testing nozzle.

Nozzle	Hole Diameter (D_h /mm)	Hole Length (L_h /mm)	Counterbore Diameter (D_c /mm)	Counterbore Length (L_c /mm)
Hole-1	0.13	0.30	0.36	0.30

2.3. Experimental Methods

2.3.1. X-ray Phase-Contrast Imaging (XPCI)

The first set of experiments was conducted at the BL40XU beamline of SPring-8 (Japan), leveraging the X-ray phase-contrast imaging (XPCI) technique to resolve near-nozzle spray dynamics. As illustrated in Figure 3, the synchrotron facility generates high-energy X-rays via relativistic electrons circulating in a storage ring. These electrons emit X-rays as they pass through bending magnets, producing a pulsed beam synchronized with the synchrotron’s 208.8 kHz revolution frequency. A mechanical shutter (8 ms opening duration) was integrated into the beam path to limit X-ray exposure, protecting the imaging system from thermal damage. XPCI captures phase shifts induced by the spray’s liquid core, which are imperceptible to conventional optical systems. To visualize these shifts, a LuAg:Ce scintillator crystal converted X-ray phase variations into visible light intensity patterns. The resulting images were reflected via a 45° mirror and recorded using a high-speed camera (Photron SA-Z,

Yamagawa, Japan) operating at 52,194 Hz (one frame per four synchrotron revolutions). The system achieved a spatial resolution of 2.22 $\mu\text{m}/\text{pixel}$ across a 1.1 mm \times 1.1 mm field of view, enabling nanoscale temporal and microscale spatial resolution of near-nozzle structures.

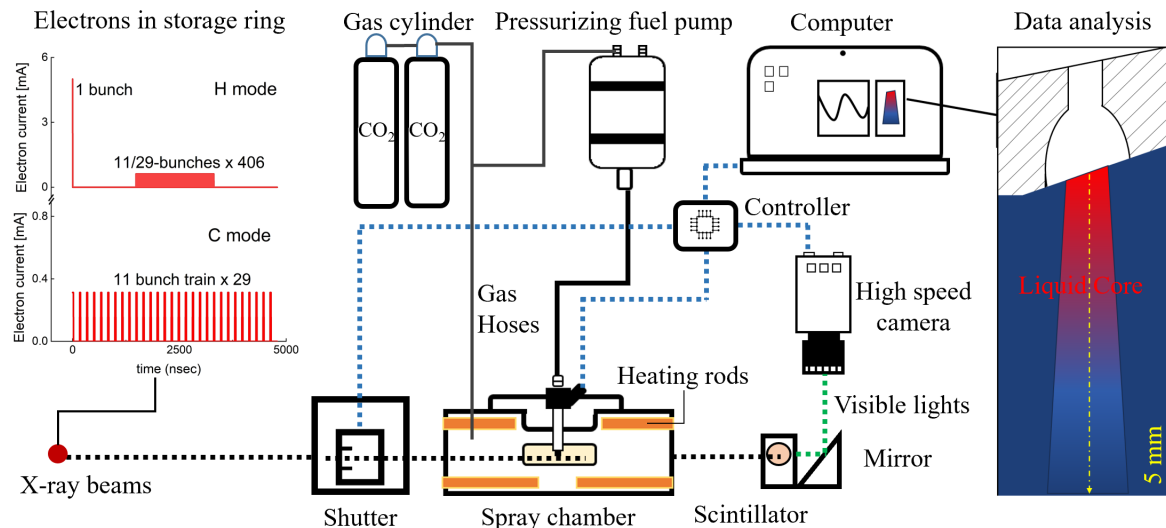


Figure 3. Experimental setup for the X-ray phase-contrast imaging.

2.3.2. Schlieren Imaging

The second experimental campaign employed a schlieren imaging setup (Figure 4) to characterize shockwave dynamics during fuel injection. The apparatus comprised a common rail injection system, a pressurized constant-volume vessel, and an LED-based schlieren optical path. Spray visualization was performed using the same Photron SA-Z high-speed camera as in the XPCI experiments, configured at 75,000 Hz with a 512 \times 496-pixel resolution (147 $\mu\text{m}/\text{pixel}$). To our knowledge, this represents the highest imaging specifications reported in analogous studies, enabling unprecedented temporal resolution of transient shockwave interactions during injection.

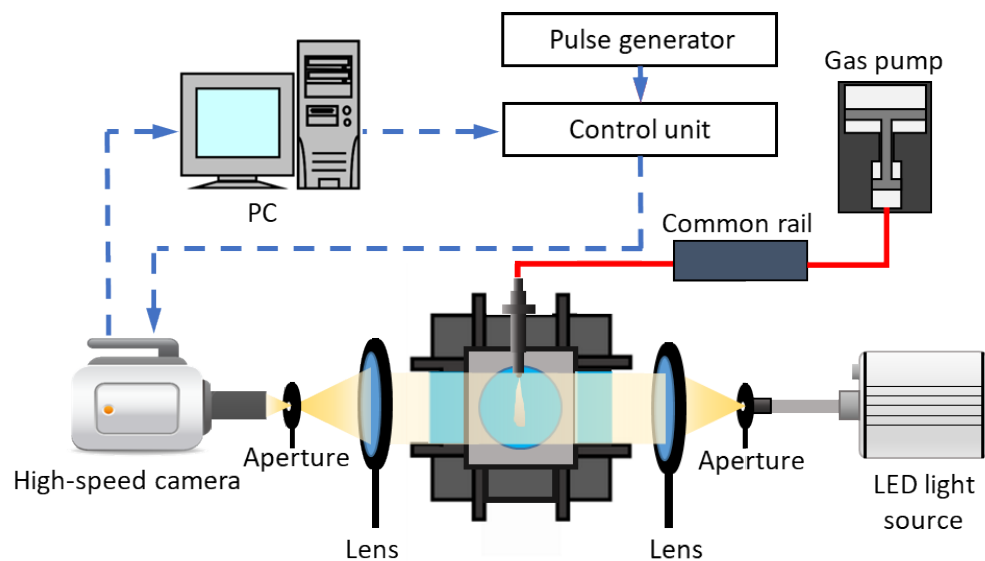


Figure 4. Experimental setup for schlieren imaging.

The spray chamber was designed with eight integrated heating rods in its metallic walls, enabling precise control of the ambient gas temperature up to 200 $^{\circ}\text{C}$ with an accuracy of ± 0.5 $^{\circ}\text{C}$, as monitored by a K-type thermocouple inserted into the injector body. Due to the chamber's compact inner volume (~ 500 mL)

and gradual heating protocol, thermal equilibrium was achieved between the chamber body (near the nozzle tip) and the ambient gas. Temperature uniformity was maintained during experiments by adopting a low sampling frequency of 0.2 Hz, while ambient pressure was monitored using a commercial pressure sensor (Keyence GP-M025, Osaka, Japan, $\pm 0.5\%$ FS accuracy). Consequently, the fuel temperature within the nozzle and the ambient gas temperature were assumed equivalent for analysis.

Five fuel temperatures were selected to span conditions from non-flash boiling to intense flash boiling. The superheat degree, defined as the ratio of ambient pressure to fuel saturation pressure P_a/P_s , was calculated using ethanol and gasoline vapor pressure data from References [25, 26], respectively, and its changing with temperature is plotted as Figure 5. Figure 5 illustrates the temperature-dependent variation of P_s for both fuels. All tests were conducted at a fixed ambient gas density of 2 kg/m^3 , with fuel injected at 25 MPa pressure over a 2 ms duration. Initial experimental parameters are summarized in Table 3.

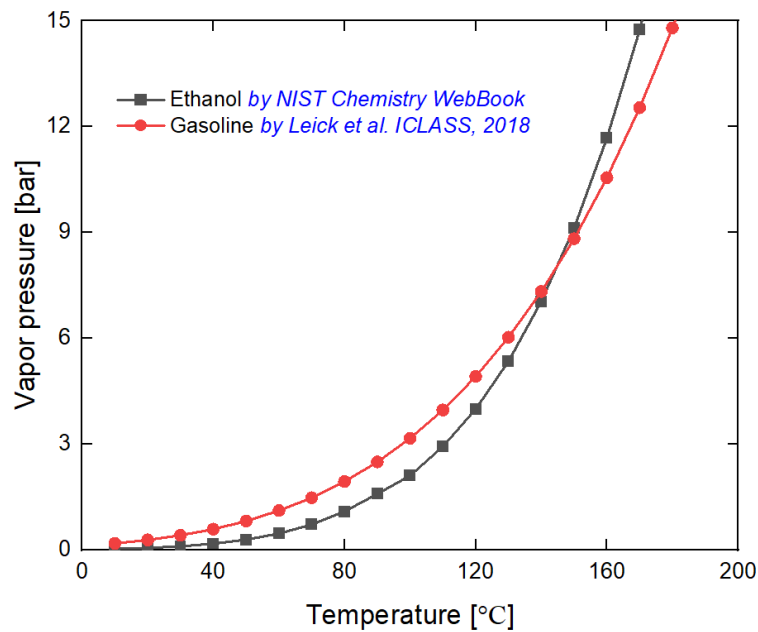


Figure 5. Vapor pressure of with different fuel temperatures [25,26].

Table 3. Initial experiment conditions.

T_f [°C]	P_a [bar]	ρ_a [kg/m ³]	$Rp = P_a/P_s$	
			Ethanol	Gasoline
20	1.10	2	20.00	3.85
65	1.27	2	2.17	0.98
100	1.40	2	0.67	0.44
150	1.59	2	0.17	0.18
200	1.78	2	0.06	0.09

2.4. Data Analysis

2.4.1. Streamwise Spray Velocity by XPCI

The streamwise spray velocity, which reflects the spray's penetrating momentum and influences mixture formation, was calculated using double-exposed X-ray phase-contrast images (Figure 6). Similar to Particle Image Velocimetry (PIV), an interrogation window was selected based on the spray pattern size to track displacement between two X-ray exposures. The time interval between exposures (143 ns) and the displacement of spray features allowed velocity calculation via self-correlation analysis. Due to the line-of-sight nature of XPCI, all features along the beam path contribute to the velocity measurement. However, auto-

correlation inherently emphasizes larger features, which dominate near the spray center, meaning the derived velocities predominantly represent the spray’s core region.

Since velocity measurement relied on imaging, the image resolution served as the primary source of uncertainty. Theoretically, the minimum measurable velocity determined by the pixel size was $1.98 \mu\text{m}/143 \text{ ns}$, equivalent to 13.9 m/s . To enhance statistical reliability, results were averaged across 10 repeated experiments (750 total frames). To enhance statistical reliability, results were averaged across 10 repeated experiments (750 total frames). A sub-pixel algorithm further refined spatial resolution by fitting Gaussian functions to correlation peaks, enabling the detection of sub-pixel displacements and improving velocity precision [27]. This methodology aligns with prior studies [28,29].

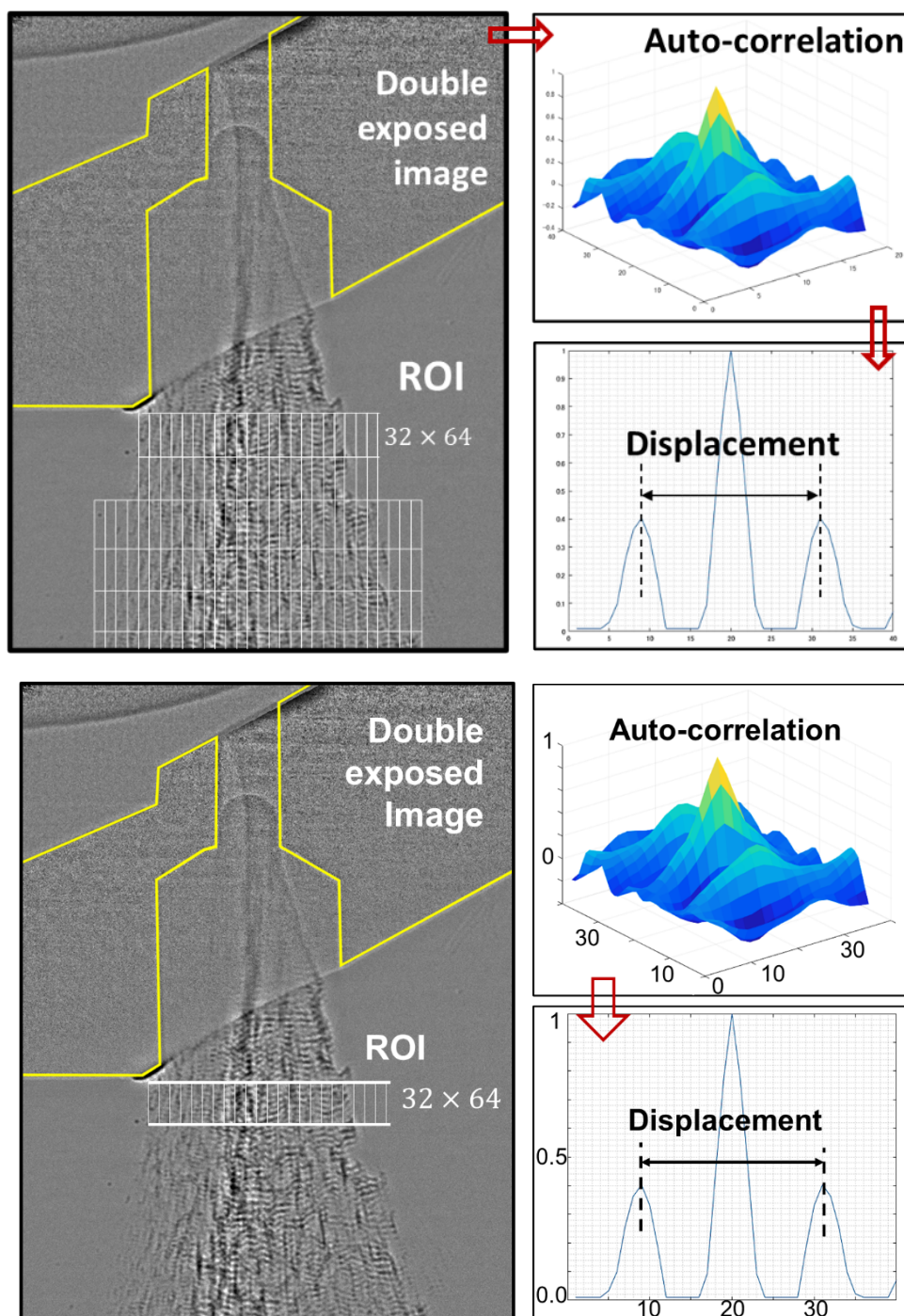


Figure 6. Analyzing method of spray velocity.

2.4.2. Sauter Mean Diameter (*SMD*) by XPCI Experiment

The Sauter mean diameter (*SMD*), a critical metric for evaluating droplet evaporation and combustion efficiency, was determined from XPCI images acquired in SPring-8's high-resolution mode. The analysis involved binarizing 2D projected images to isolate droplet boundaries, as shown in Figure 7, followed by a 2D-to-3D conversion assuming axisymmetric circular cross-sections [30]. While this method may introduce errors for arbitrarily deformed droplets, such deviations are minimal in well-developed spray regions. *SMD* was calculated within a region of interest (ROI) as the ratio of total droplet volume to total surface area, consistent with established approaches [31,32]. The *SMD* in a certain ROI is then calculated by the droplet volume (D_{volume_n}) divided by the droplet surface area (D_{area_n}) as expressed in Equation (1), where *n* denotes the *n*th detected droplet within the ROI.

$$SMD = \frac{\sum_1^n D_{\text{volume}_n}^3}{\sum_1^n D_{\text{area}_n}^2} \quad (1)$$

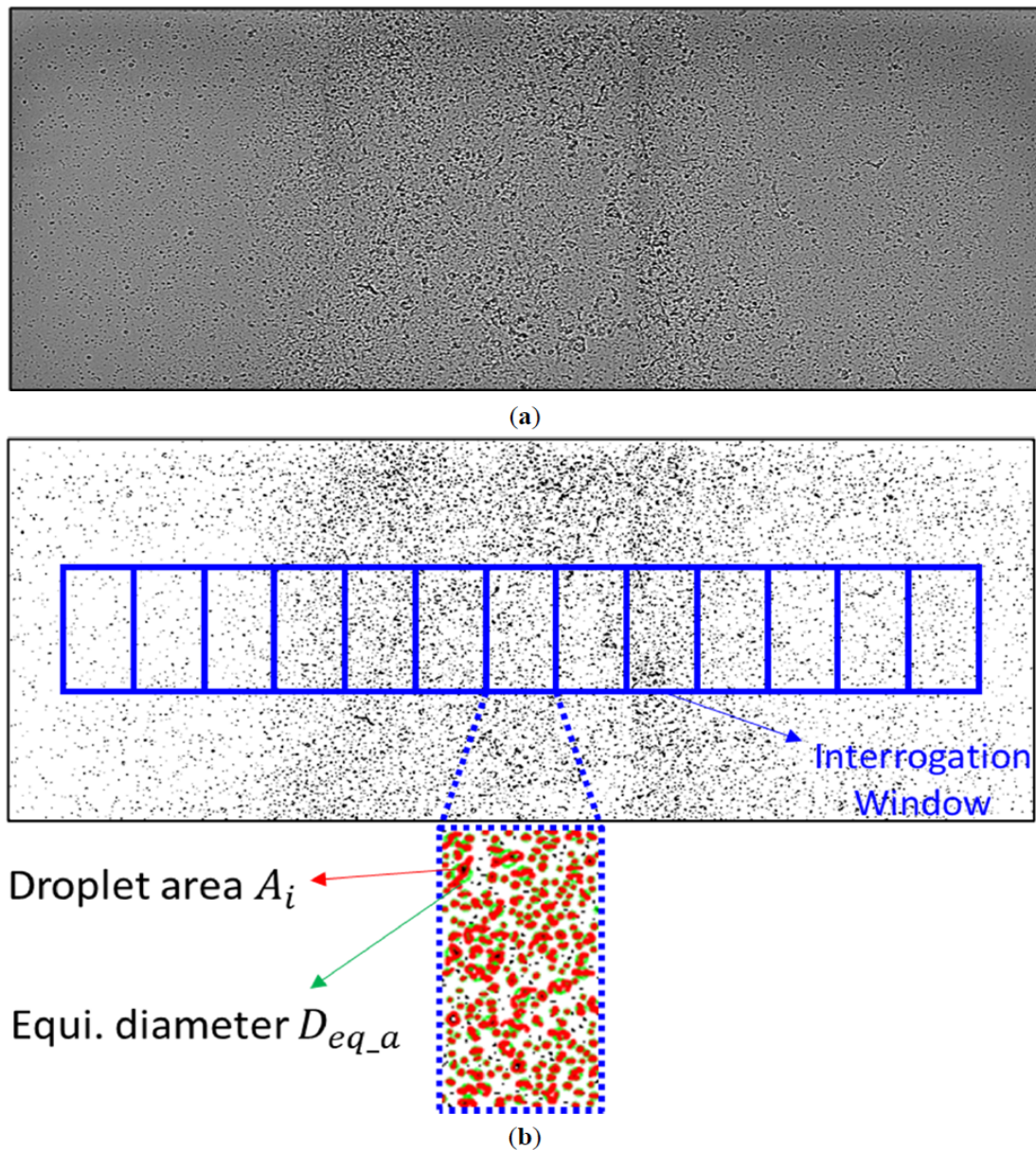


Figure 7. X-ray single-exposure image analyzing method for *SMD* measurement: (a) processed image; (b) binarized image.

2.4.3. Spray tip Penetration by Schlieren Imaging

Spray tip penetration and spray area were extracted from schlieren images using a custom processing pipeline (Figure 8). Raw images were first normalized against a background reference (Figure 8b) to eliminate fixed-pattern noise. False-color mapping (Figure 8d) enhanced grayscale gradients, which correlate with fuel density variations and evaporation heterogeneity. Adaptive thresholding [33] was then used to convert the enhanced images into binary form (Figure 8e), enabling quantification of spray tip penetration (maximum axial reach) and spray area (2D projected footprint). These parameters collectively characterize the spray's penetration capability and spatial dispersion.

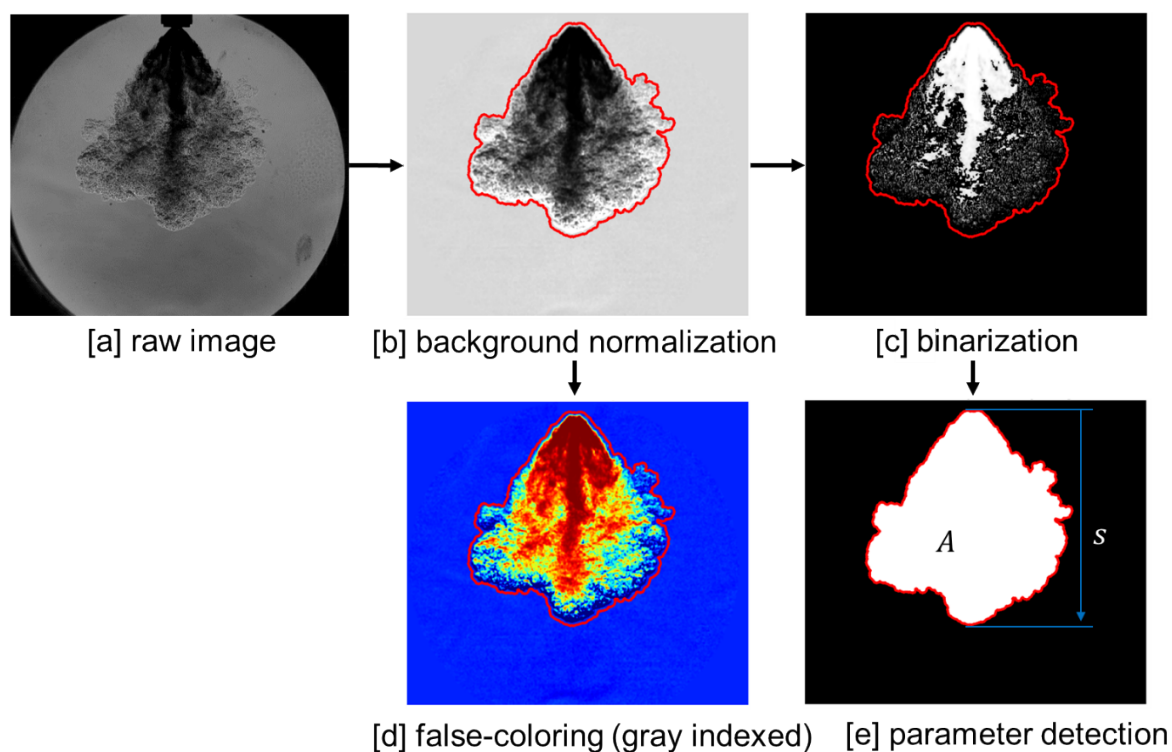


Figure 8. Image processing and data analysis.

3. Experimental Results and Discussions

Figure 9 presents processed schlieren images of ethanol and gasoline sprays at varying temperatures, captured 1 ms after the start of injection (ASOI). The color spectrum encodes spray density, with red hues indicating regions of higher fuel concentration and reduced light transmission. These images provide direct visual evidence of flash-boiling behavior and its influence on spray morphology. At room temperature, both fuels exhibit elongated spray structures with distinct spacing between individual plumes. As the fuel temperature rises to 100 °C, spray penetration shortens, and plume spacing diminishes—particularly for ethanol. This aligns with ethanol's lower saturation temperature (~78 °C), which promotes rapid vaporization post-injection. At 200 °C, ethanol sprays display further contraction, complete plume merging, and upward curling at the spray edges (evident in sequential frames), consistent with flash-boiling dynamics.

These observations confirm ethanol's transition to flash-boiling conditions at this temperature. In contrast, gasoline sprays at 200 °C show plume coalescence but lack the characteristic edge curling. This divergence arises from gasoline's multi-component composition, where varying volatilities among hydrocarbons suppress homogeneous phase change. Instead, localized vaporization of lighter fractions likely dominates, moderating the intensity of flash-boiling effects. The absence of upward curling suggests incomplete superheating or heterogeneous bubble nucleation within the spray, underscoring the challenges in achieving uniform flash boiling with complex fuel blends.

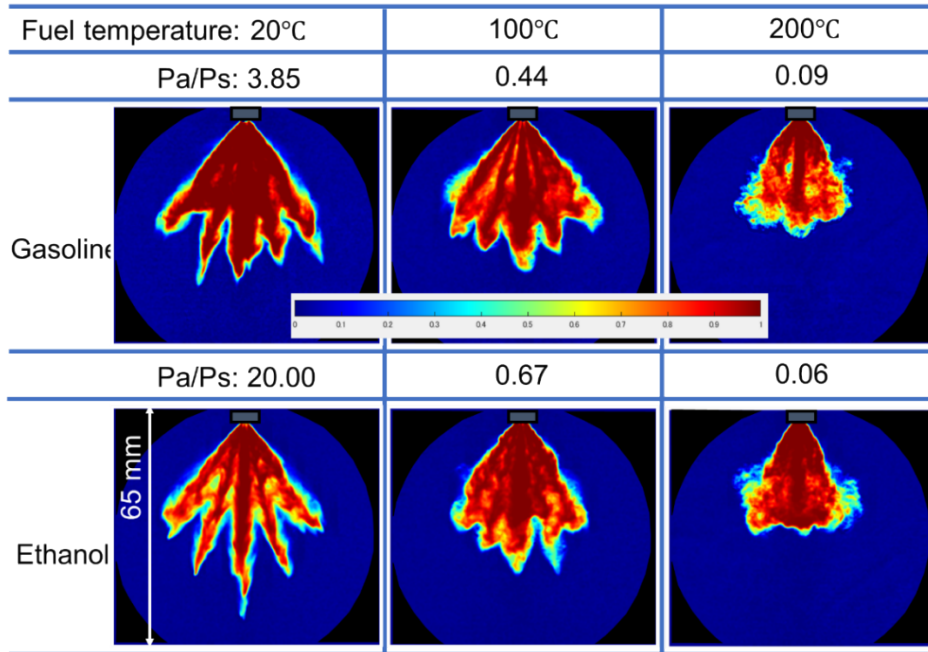


Figure 9. Spray morphology in various fuel temperatures measured by schlieren imaging.

Figure 10 illustrates the variation in spray tip penetration with superheat degree (fuel temperature) for both fuels. The spray tip penetration values correspond to measurements taken 1 ms after the start of injection (ASOI). As shown, the spray tip penetration decreases progressively with increasing superheat degree, exhibiting an approximately logarithmic proportionality to P_d/P_s . In this study, the experimental P_d/P_s conditions differed between gasoline and ethanol. However, under comparable P_d/P_s ratios, the spray tip penetration of ethanol and gasoline appears relatively similar. While differences in fuel density (ethanol is 8% higher) and latent heat of vaporization (ethanol is 175% higher) contribute to deviations, the influence of on spray tip penetration remains dominant.

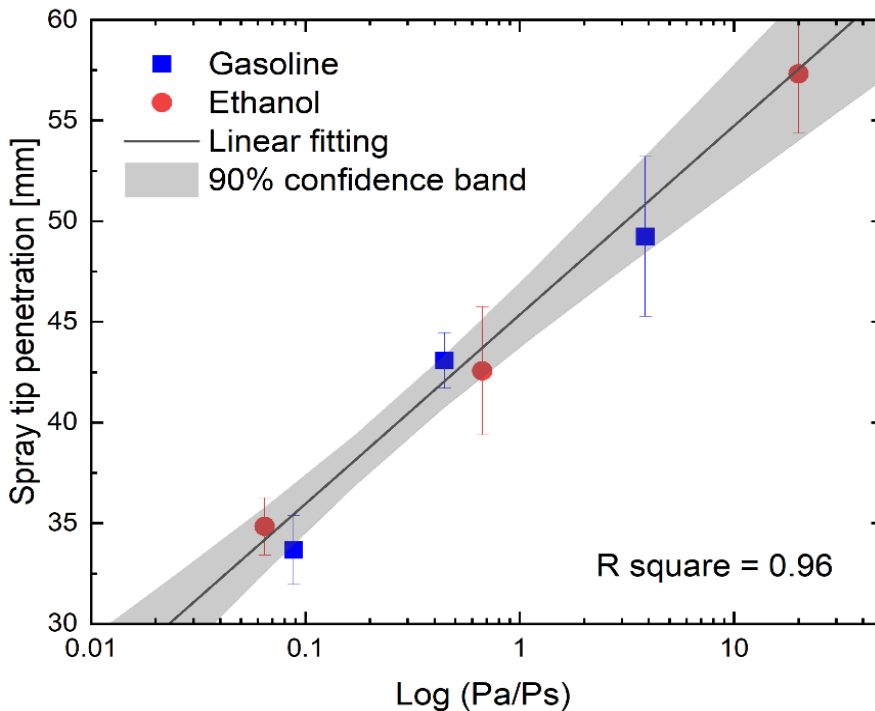


Figure 10. Spray tip penetration vs. $\log(P_d/P_s)$ at ASOI 1.0 ms.

To further investigate the near-nozzle dynamics under these conditions, XPCI was employed. Figure 11 compares near-nozzle ethanol and gasoline sprays at varying fuel temperatures, with data acquired from Hole-1 (vertically oriented nozzle). Notably, even at 200 °C—a temperature well above ethanol’s saturation point (~78 °C)—a continuous liquid core persists in ethanol’s superheated spray. This observation contrasts with conventional expectations of rapid atomization under flash-boiling conditions. Moreover, the XPCI images reveal no significant structural differences between the liquid cores of ethanol and gasoline sprays, despite ethanol’s higher volatility and distinct thermophysical properties.

A critical constraint of XPCI must be emphasized: the technique visualizes phase interfaces (liquid-gas boundaries) but cannot resolve fully vaporized regions. Thus, while XPCI captures the liquid core’s persistence and its disintegration dynamics, it inherently excludes gaseous-phase structures from analysis. This limitation underscores the method’s utility in tracking the process of liquid core collapse during flash boiling, rather than its final vaporized state.

The persistence of the liquid core in superheated ethanol sprays suggests that flash boiling does not instantaneously disrupt the jet’s continuity. Potential explanations include localized cooling from rapid vaporization, which may suppress complete phase change, or the dominance of inertial forces over bubble growth near the nozzle. These hypotheses warrant further investigation, particularly in downstream regions of the spray where secondary atomization and vaporization dominate.

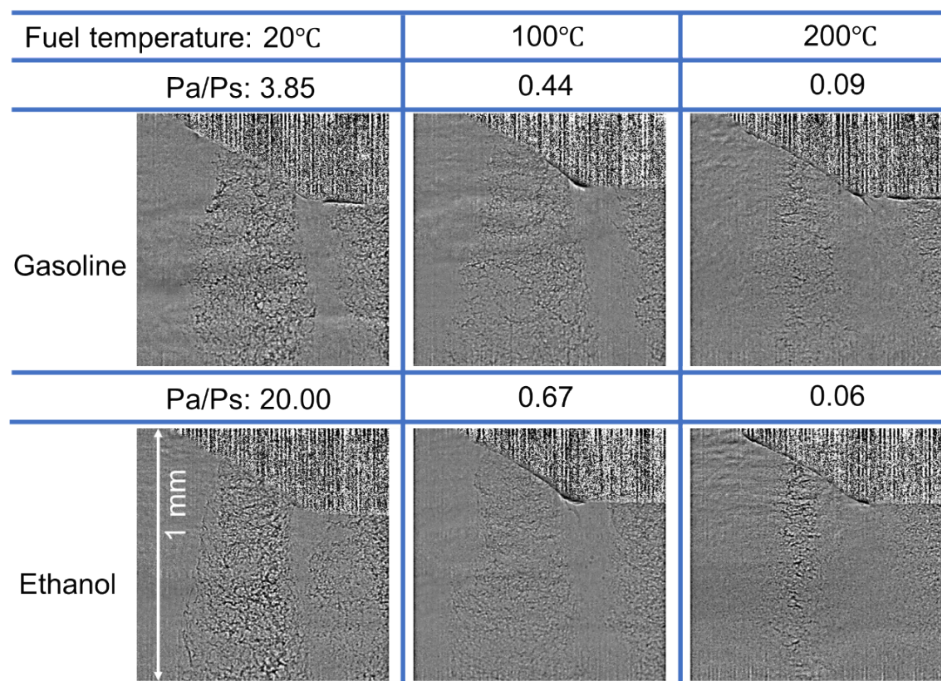


Figure 11. Near nozzle spray morphology in various fuel temperatures observed by XPCI.

Droplet size distributions were measured 1.5 mm downstream of the nozzle exit under both flash-boiling (200 °C) and non-flash-boiling conditions (20 °C), as shown in Figure 12. The *SMD* for non-flash-boiling conditions was 22.6 μm at 20 °C, compared to 13.3 μm under flash-boiling conditions. Under flash boiling, the droplet diameters exhibit a narrow distribution, predominantly concentrated between 4–12 μm with a distinct peak at 5 μm. In contrast, non-flash-boiling sprays display a broader size range, including a higher proportion of larger droplets (>12 μm).

The narrowed droplet size distribution under flash boiling aligns with expectations of enhanced atomization from vapor bubble nucleation and collapse, yet micron-scale droplets persist 1.5 mm downstream—indicating incomplete phase change despite superheating. This liquid core persistence reflects competing mechanisms: (1) localized cooling via rapid latent heat absorption (consistent with Naber & Siebers’ thermal boundary layer theory [34]), which temporarily suppresses vaporization near the nozzle; and (2) inertial dominance at high Reynolds numbers ($Re \sim 10^4$) where momentum exceeds bubble growth rates (per Reitz’s

jet stability analysis [35]). While our current data cannot isolate the dominant mechanism, future work will resolve this ambiguity through phase-resolved CFD simulations (using present XPCI velocity data as boundary conditions) coupled with evaporative mass transfer models, directly addressing this knowledge gap.

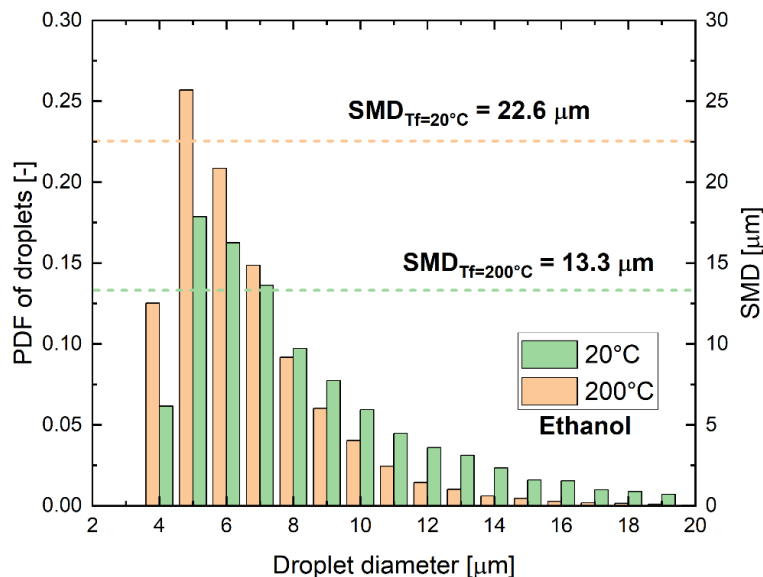


Figure 12. Comparison of droplet sizes between flash-boiling and non-flash-boiling conditions.

Figure 13 examines near-nozzle spray velocities under varying fuel temperatures, providing insights into momentum dynamics during flash boiling. The average axial droplet velocity at 0.5 mm from the nozzle exit correlates with predictions from Bernoulli’s principle, as shown in Figure 13a, where velocity (u) scales with the pressure differential and fuel density ($1/\rho_f$):

$$u = \sqrt{\frac{2(P_{in} - P_a)}{\rho_f}} = \sqrt{\frac{2\Delta P}{\rho_f}} \tag{2}$$

Notably, the persistence of this linear trend even at 200 °C—where flash boiling occurs—indicates that a coherent liquid core survives near the nozzle exit, maintaining momentum continuity despite vaporization.

At elevated temperatures, the radial velocity profile sharpens significantly, as shown in Figure 13b. For instance, at 200 °C, the jet width narrows by approximately 40% compared to room temperature, while peak axial velocities increase by ~25%. This narrowing reflects rapid fuel evaporation, which reduces the spray’s lateral momentum and concentrates the remaining liquid phase into a tighter, faster-moving core. The diminished streamwise penetration observed in prior results (Figure 9) can thus be attributed to two factors. Firstly, evaporation reduces the total liquid mass available to sustain forward momentum. Secondly, accelerated axial velocities prioritize kinetic energy over spatial dispersion.

Figure 14 examines the axial velocity evolution of ethanol and gasoline sprays from the nozzle exit to downstream regions. For ethanol (upper panel), elevated fuel temperatures induce a slight velocity increase within the first 0.5 mm downstream, likely driven by vapor expansion during flash boiling. Beyond this region, the spray transitions into a dispersed droplet cloud, yet individual droplets retain high velocities (~80–120 m/s), indicating conserved momentum despite liquid core disintegration. In contrast, gasoline droplets (lower panel) penetrate further downstream, a behavior attributed to its lower latent heat of vaporization (175% less than ethanol) and multi-component composition. Both fuels exhibit a pronounced velocity decline in the 1.0–1.5 mm zone, marking a transition from inertial dominance to aerodynamic and phase-change-driven deceleration—a critical region for secondary breakup and mixing. These velocity profiles deviate from classical single-phase jet models, emphasizing the need for two-phase formulations that account for vapor-liquid interactions during flash boiling.

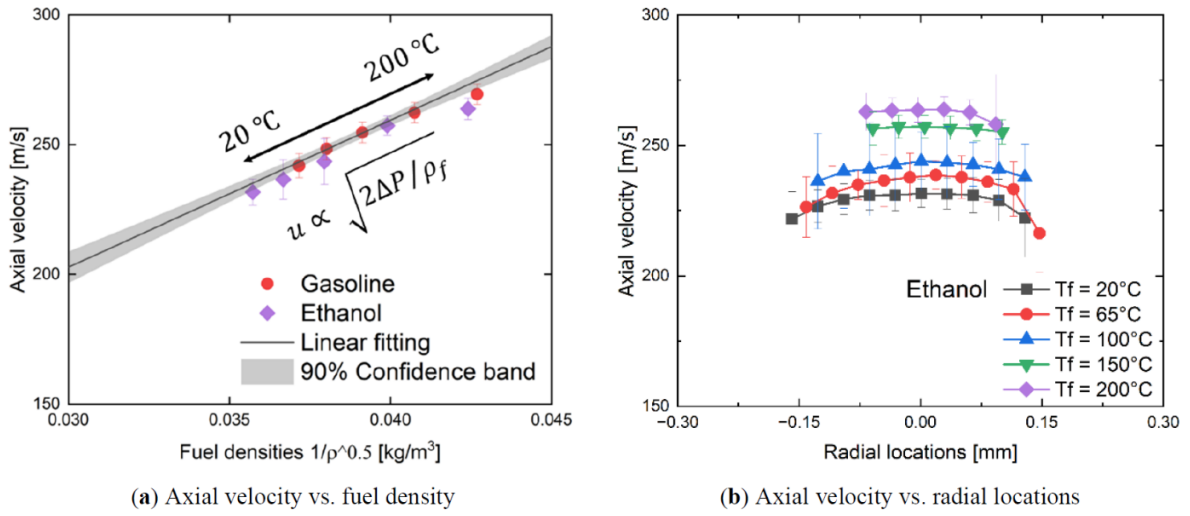


Figure 13. Nozzle-exit spray velocity of different fuels in various fuel temperatures.

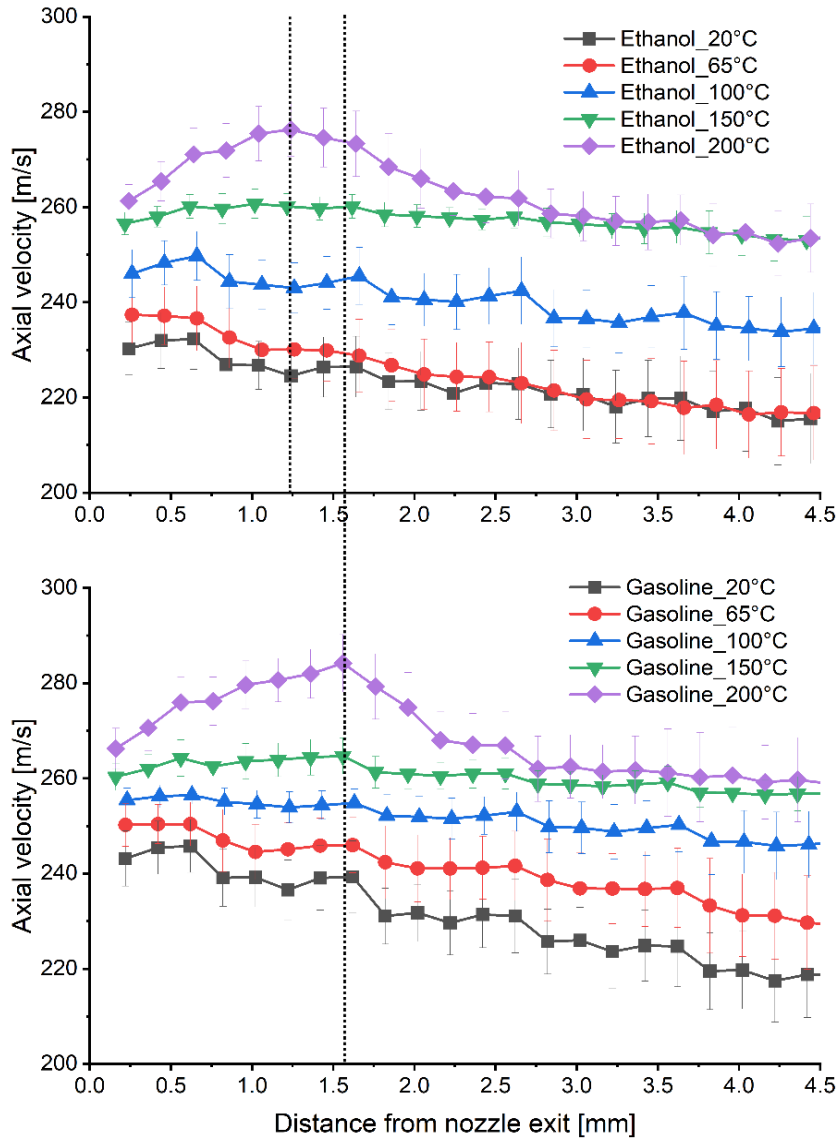


Figure 14. Axial velocity evolution of ethanol and gasoline sprays from the nozzle exit to downstream regions.

Revisiting the flash-boiling breakup mechanism proposed by Chang et al. [10]—where vapor bubbles explosively rupture upon exiting the nozzle, driving radial spray expansion—we analyzed radial velocity profiles under both non-flash and flash-boiling conditions. Experimental results (Figure 15) confirm a pronounced increase in radial velocity during flash boiling, validating Chang et al.’s hypothesis of bubble-driven atomization. The radial velocity asymmetry observed (right > left) on flash boiling condition likely stems from aerodynamic interference between adjacent spray plumes, as the left-side spray is partially obstructed by neighboring jet interactions.

This radial momentum surge aligns with the rapid bubble growth and collapse described in their model, which converts axial momentum into radial dispersion. However, our findings also reveal limitations in existing frameworks: while Chang et al.’s mechanism explains radial expansion, it does not fully account for the persistent liquid core observed in XPCI results (Figure 9), suggesting inertial forces partially counteract bubble-induced fragmentation near the nozzle. To resolve this discrepancy, future work must integrate near-nozzle liquid-core dynamics (e.g., velocity continuity, thermal non-equilibrium) into flash-boiling models, bridging the gap between microscale bubble behavior and macroscale spray morphology. Such advancements will refine predictive tools for optimizing fuel-air mixing and mitigating plume-to-plume interference in multi-hole injectors.

While the current study did not experimentally vary nozzle geometry (e.g., orifice diameter, cone angle), prior work (e.g., Du et al. [36]; Jin et al. [37]; Zhai et al. [38]) suggests that geometric parameters significantly influence spray characteristics, including droplet size and penetration. However, their effects on near-nozzle liquid core dynamics under flash-boiling conditions remain unresolved. Future studies will integrate parametric nozzle designs with XPCI to systematically unravel these mechanisms, providing actionable guidelines for injector optimization to mitigate tip wetting while enhancing atomization efficiency.

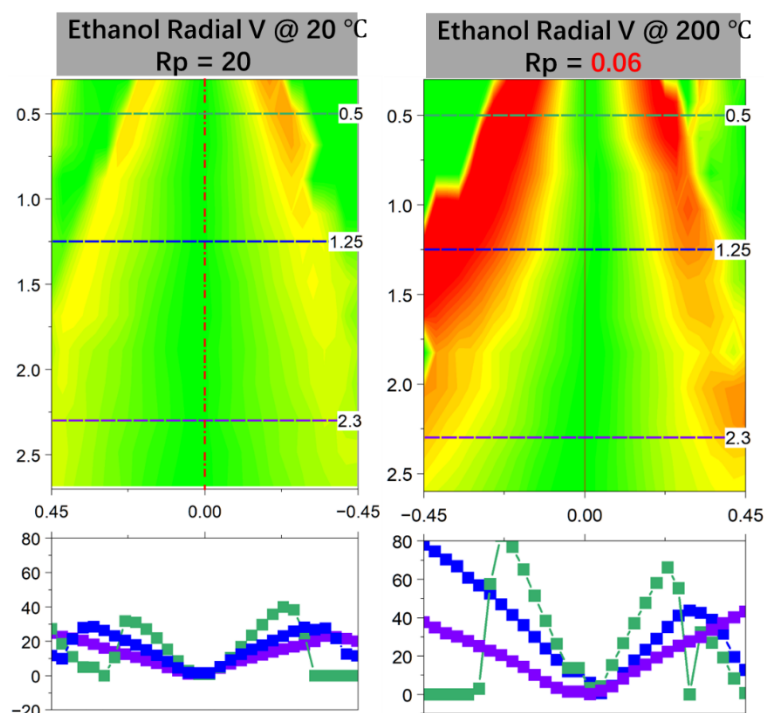


Figure 15. Flash boiling effect on spray radial velocity.

4. Conclusions

This paper aims to investigate and reveal the intricate dynamics of superheated sprays and their underlying mechanisms, utilizing the advantages of X-ray phase-contrast imaging (XPCI) and schlieren imaging setup. Ethanol and gasoline were used for a comparison. The key findings can be summarized as bellow:

- (1) Ethanol sprays exhibit definitive flash-boiling behavior at 200 °C, characterized by plume merging, upward curling, and reduced penetration. Gasoline, however, shows no clear flash-boiling signatures (e.g., edge curling) due to its multi-component composition, which moderates homogeneous phase change.
- (2) XPCI imaging demonstrates that even under intense superheating, a coherent liquid core persists near the nozzle exit for both fuels. This challenges assumptions of instantaneous atomization in flash-boiling models and highlights the role of inertial forces in delaying liquid-core disintegration.
- (3) Flash boiling narrows droplet size distributions (4–12 μm for ethanol at 200 °C), indicating enhanced atomization. However, residual droplets near the nozzle (~1.5 mm downstream) suggest incomplete vaporization, likely due to localized cooling from rapid latent heat absorption.
- (4) Axial velocities correlate inversely with fuel density, while radial velocities surge under flash boiling. The coexistence of high-velocity liquid cores and vaporizing peripheries underscores the multi-phase nature of flash-boiling sprays. While bubble nucleation enhances atomization, residual droplets and plume interactions pose risks of tip wetting and wall impingement.

Author Contributions: W. H.: Conceptualization, methodology, software, validation, formal analysis, data curation, visualization, investigation, writing—original draft preparation; H. L.: supervision, project administration, funding acquisition, writing—review and editing. All authors have read and agreed to the published version of the manuscript.

Funding: This research received no external funding.

Data Availability Statement: Not applicable.

Acknowledgments: We also thank Raditya Hendra Pratama of National Research and Innovation Agency (BRIN) and other collaborators (Gong Huifeng, Senzai Yusuke) for their assistance during the experiments.

Conflicts of Interest: The authors declare no conflict of interest.

Reference

1. Li, X.; Wang, S.; Yang, S.; Qiu, S.; Sun, Z.; Hung, D.L.; Xu, M. A review on the recent advances of flash boiling atomization and combustion applications. *Prog. Energy Combust. Sci.* **2024**, *100*, 101119. <https://doi.org/10.1016/j.pecs.2023.101119>.
2. Xu, M. Combustion Improved by Using Flash Boiling Sprays in an Ethanol-Gasoline Optical Engine under Cold Operating Conditions. *Energy Fuels* **2021**, *35*, 10134–10145. <https://doi.org/10.1021/acs.energyfuels.1c00739>.
3. Wu, S.; Yang, S.; Wooldridge, M.; Xu, M. Experimental study of the spray collapse process of multi-hole gasoline fuel injection at flash boiling conditions. *Fuel* **2019**, *242*, 109–123. <https://doi.org/10.1016/j.fuel.2019.01.027>.
4. Zeng, W.; Xu, M.; Zhang, M.; Zhang, Y.; Cleary, D.J. Macroscopic characteristics for direct-injection multi-hole sprays using dimensionless analysis. *Exp. Therm. Fluid. Sci.* **2012**, *40*, 81–92. <https://doi.org/10.1016/j.expthermflusci.2012.02.003>.
5. Zeng, W.; Xu, M.; Zhang, Y.; Wang, Z. Laser sheet droplet sizing of evaporating sprays using simultaneous LIEF/MIE techniques. *Proc. Combust. Inst.* **2013**, *34*, 1677–1685. <https://doi.org/10.1016/j.proci.2012.07.061>.
6. Wu, S.; Gandhi, A.; Li, H.; Meinhart, M. Experimental and numerical study of the effects of nozzle taper angle on spray characteristics of GDI multi-hole injectors at cold condition. *Fuel* **2020**, *275*, 117888. <https://doi.org/10.1016/j.fuel.2020.117888>.
7. Wu, S.; Xu, M.; Hung, D.L.S.; Pan, H. In-nozzle flow investigation of flash boiling fuel sprays. *Appl. Therm. Eng.* **2017**, *117*, 644–651. <https://doi.org/10.1016/j.applthermaleng.2016.12.105>.
8. Huang, W.; Gong, H.; Moon, S.; Wang, J.; Murayama, K.; Taniguchi, H.; Arima, T.; Arioka, A.; Sasaki, Y. Nozzle Tip Wetting in GDI Injector at Flash-boiling Conditions. *Int. J. Heat. Mass. Transf.* **2021**, *169*, 120935. <https://doi.org/10.1016/j.ijheatmasstransfer.2021.120935>.
9. Xiao, D.; Qiu, S.; Zhang, X.; Zhang, Y.; Li, X.; Hung, D.; Xu, M. Dynamic behavior and mechanism analysis of tip wetting process under flash boiling conditions. *Fuel* **2022**, *307*, 121773. <https://doi.org/10.1016/j.fuel.2021.121773>.
10. Chang, M.; Lee, Z.; Park, S.S.; Park, S.S. Characteristics of flash boiling and its effects on spray behavior in gasoline direct injection injectors: A review. *Fuel* **2020**, *271*, 117600. <https://doi.org/10.1016/j.fuel.2020.117600>.
11. Dong, X.; Yang, J.; Hung, D.L.S.; Li, X.; Xu, M. Effects of flash boiling injection on in-cylinder spray, mixing and combustion of a spark-ignition direct-injection engine. *Proc. Combust. Inst.* **2019**, *37*, 4921–4928. <https://doi.org/10.1016/j.proci.2018.09.014>.
12. Loureiro, D.D.; Reutzsch, J.; Kronenburg, A.; Weigand, B.; Vogiatzaki, K. Primary breakup regimes for cryogenic flash atomization. *Int. J. Multiph. Flow* **2020**, *132*, 103405. <https://doi.org/10.1016/j.ijmultiphaseflow.2020.103405>.
13. Loureiro, D.D.; Kronenburg, A.; Reutzsch, J.; Weigand, B.; Vogiatzaki, K. Droplet size distributions in cryogenic flash atomization. *Int. J. Multiph. Flow* **2021**, *142*, 103705. <https://doi.org/10.1016/j.ijmultiphaseflow.2021.103705>.
14. Oza, R.D. On the Mechanism of Flashing Injection of Initially Subcooled Fuels. *J. Fluids Eng.* **1984**, *106*, 105–109. <https://doi.org/10.1115/1.3242383>.

15. Bar-Kohany, T.; Levy, M. State of the art review of flash-boiling atomization. *At. Sprays* **2016**, *26*, 1259–1305. <https://doi.org/10.1615/AtomizSpr.2016015626>.
16. Duke, D.; Swantek, A.; Kastengren, A.; Fezzaa, K.; Powell, C. Recent Developments in X-ray Diagnostics for Cavitation. *SAE Int. J. Fuels Lubr.* **2015**, *8*, 135–146. <https://doi.org/10.4271/2015-01-0918>.
17. Kastengren, A.; Powell, C. F.; Liu, Z.; Wang, J. *Time Resolved, Three Dimensional Mass Distribution of Diesel Sprays Measured with X-ray Radiography*; SAE Technical Papers; SAE: Warrendale, PA, USA, 2009. <https://doi.org/10.4271/2009-01-0840>.
18. Huang, W.; Pratama, R.H.; Oguma, M.; Kinoshita, K.; Takeda, Y.; Suzuki, S. Spray dynamics of synthetic dimethyl carbonate and its blends with gasoline. *Fuel* **2023**, *341*, 127696. <https://doi.org/10.1016/j.fuel.2023.127696>.
19. Wang, X.; Pan, J.; Wu, J.; Liu, Z. Surface tension of dimethoxymethane and methyl tert-butyl ether. *J. Chem. Eng. Data* **2006**, *51*, 1394–1397. <https://doi.org/10.1021/je060097q>.
20. Ramos-Estrada, M.; Iglesias-Silva, G.A.; Hall, K.R. Experimental measurements and prediction of liquid densities for n-alkane mixtures. *J. Chem. Thermodyn.* **2006**, *38*, 337–347. <https://doi.org/10.1016/j.jct.2005.05.020>.
21. Schifter, I.; González, U.; González-Macías, C. Effects of ethanol, ethyl-tert-butyl ether and dimethyl-carbonate blends with gasoline on SI engine. *Fuel* **2016**, *183*, 253–261. <https://doi.org/10.1016/j.fuel.2016.06.051>.
22. Huang, W.; Oguma, M.; Kinoshita, K.; Abe, Y.; Tanaka, K. Investigating Spray Characteristics of Synthetic Fuels: Comparative Analysis with Gasoline. *Int. J. Automot. Manuf. Mater.* **2024**, *3*, 2. <https://doi.org/10.53941/ijamm.2024.100008>
23. Wu, P.; Xuan, T.; He, Z.; Shao, Z.; Wang, Q.; Payri, R. A comparative study on combustion characteristics of PPC and RCCI combustion modes in an optical engine with renewable fuels. *Fuel* **2025**, *381*, 133361. <https://doi.org/10.1016/j.fuel.2024.133361>.
24. Chang, F.; Luo, H.; Zhai, C.; Jin, Y.; Xiong, P.; Wang, J.; Song, B.; Zhang, J.; Nishida, K. Experimental investigation of fuel adhesion from wall-impinging spray with various injection mass ratios. *Exp. Therm. Fluid. Sci.* **2025**, *163*, 111403. <https://doi.org/10.1016/j.expthermflusci.2024.111403>.
25. Properties of Ethanol at NIST. Available online: <https://webbook.nist.gov/cgi/cbook.cgi?ID=C64175&Mask=4> (accessed on 13 March 2024).
26. Leick, P.; Bork, B.; Geiler, J.N. Experimental characterization of tip wetting in gasoline DI injectors. In Proceedings of the ICLASS 2018—14th International Conference on Liquid Atomization and Spray Systems, Chicago, IL, USA, 22–26 July 2018.
27. Nobach, H.; Honkanen, M. Two-dimensional Gaussian regression for sub-pixel displacement estimation in particle image velocimetry or particle position estimation in particle tracking velocimetry. *Exp. Fluids* **2005**, *38*, 511–515. <https://doi.org/10.1007/s00348-005-0942-3>.
28. Huang, W.; Moon, S.; Ohsawa, K. Near-nozzle dynamics of diesel spray under varied needle lifts and its prediction using analytical model. *Fuel* **2016**, *180*, 292–300. <https://doi.org/10.1016/j.fuel.2016.04.042>.
29. Gao, Y.; Huang, W.; Pratama R.H. Influence of hydraulic flip on spray uniformity and dynamics in Gasoline Direct Injection nozzles. *Int. J. Heat. Mass. Transf.* **2025**, *242*, 126848. <https://doi.org/10.1016/j.ijheatmasstransfer.2025.126848>.
30. Sechenyh, V.; Duke, D.J.; Swantek, A.B.; Matusik, K.E.; Kastengren, A.L.; Powell, C.F.; Viera, A.; Payri, R.; Crua, C. Quantitative analysis of dribble volumes and rates using three-dimensional reconstruction of X-ray and diffused back-illumination images of diesel sprays. *Int. J. Engine Res.* **2020**, *21*, 43–54. <https://doi.org/10.1177/1468087419860955>.
31. Gong, H.; Huang, W.; Gao, Y.; Wang, J.; Arioka, A.; Sasaki, Y. End-of-injection fuel dribbling dynamics of multi-hole GDI injector. *Fuel* **2022**, *317*, 123406. <https://doi.org/10.1016/j.fuel.2022.123406>.
32. Pratama, R. H.; Huang, W.; Moon, S. Unveiling needle lift dependence on near-nozzle spray dynamics of diesel injector. *Fuel* **2021**, *285*, 119088. <https://doi.org/10.1016/j.fuel.2020.119088>.
33. Otsu, N. Threshold selection method from gray-level histograms. *IEEE Trans. Syst. Man. Cybern.* **1979**, *9*, 62–66. <https://doi.org/10.1109/TSMC.1979.4310076>.
34. Naber, J.D.; Siebers, D.L. *Effects of Gas Density and Vaporization on Penetration and Dispersion of Diesel Sprays*; SAE Technical Papers; SAE: Warrendale, PA, USA, 1996. <https://doi.org/10.4271/960034>.
35. Reitz, R.D. Mechanisms of Atomization Processes in High-Pressure Vaporizing Sprays. *At. Spray. Technol.* **1987**, *3*, 309–337.
36. Du, W.; Lou, J.; Liu, F. *Effects of Nozzle Hole Diameter on Diesel Sprays in Constant Injection Mass Condition*; SAE Technical Papers; SAE: Warrendale, PA, USA, 2017. <https://doi.org/10.4271/2017-01-2300>.
37. Jin, Y.; Zhang, Y.; Dong, P.; Zhai, C.; Nishida, K.; Wang, Y.; Leng, X. Diesel spray characteristics of multi-hole injectors under geometrical similarity condition. *At. Sprays* **2025**, *35*, 19–45. <https://doi.org/10.1615/ATOMIZSPR.2025053971>.
38. Zhai, C.; Liu, E.; Zhang, G.; Xing, W.; Chang, F.; Jin, Y.; Luo, H.; Nishida, K.; Ogata, Y. Similarity and normalization study of fuel spray and combustion under ultra-high injection pressure and micro-hole diameter conditions—spray characteristics. *Energy* **2024**, *288*, 129684. <https://doi.org/10.1016/j.energy.2023.129684>.